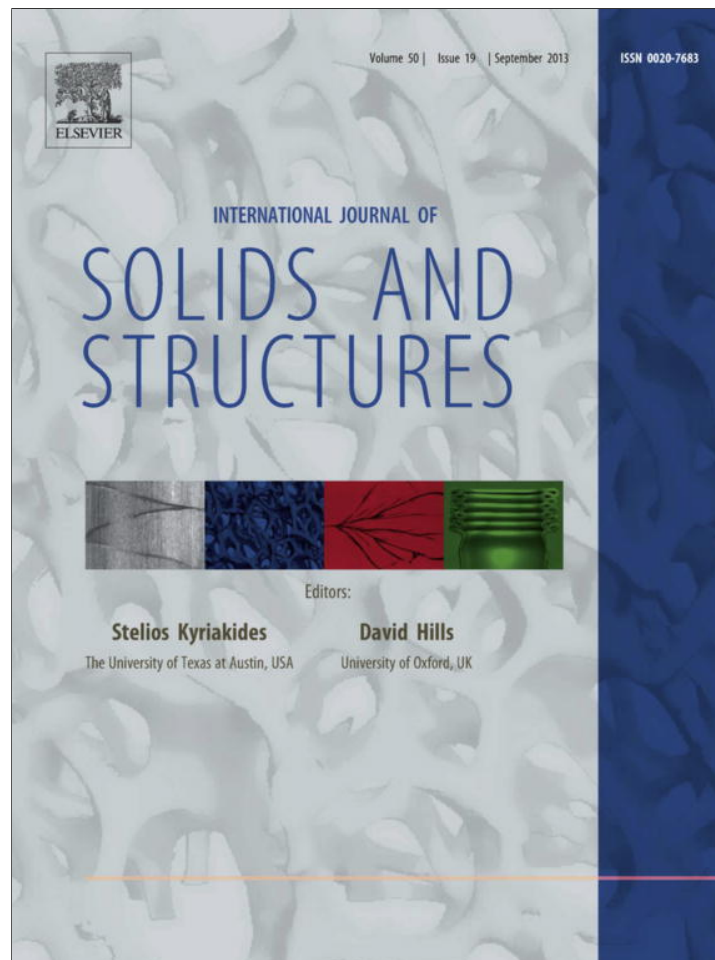


Provided for non-commercial research and education use.
Not for reproduction, distribution or commercial use.



This article appeared in a journal published by Elsevier. The attached copy is furnished to the author for internal non-commercial research and education use, including for instruction at the authors institution and sharing with colleagues.

Other uses, including reproduction and distribution, or selling or licensing copies, or posting to personal, institutional or third party websites are prohibited.

In most cases authors are permitted to post their version of the article (e.g. in Word or Tex form) to their personal website or institutional repository. Authors requiring further information regarding Elsevier's archiving and manuscript policies are encouraged to visit:

<http://www.elsevier.com/authorsrights>



Contents lists available at SciVerse ScienceDirect

International Journal of Solids and Structures

journal homepage: www.elsevier.com/locate/ijsolstr

Phase-field simulation of stress-induced martensitic phase transformations at large strains

Vladimir A. Levin^a, Valery I. Levitas^{b,*}, Konstantin M. Zingerman^{c,d}, Eugene I. Freiman^d^a Department of Mechanics and Mathematics, Lomonosov Moscow State University, Moscow 119899, Russian Federation^b Iowa State University, Departments of Aerospace Engineering, Mechanical Engineering, and Material Science and Engineering, Ames, IA 50011, USA^c Department of Applied Mathematics and Cybernetics, Tver State University, Tver 170100, Russian Federation^d FIDESYS Limited, Scientific Park, Lomonosov Moscow State University, Moscow 119991, Russian Federation

ARTICLE INFO

Article history:

Received 20 March 2013

Received in revised form 30 April 2013

Available online 16 May 2013

Keywords:

Martensitic phase transformation

Phase field approach

Finite element method

Nucleation at nanovoids

ABSTRACT

A complete system of coupled phase-field and mechanical equations for the simulation of multivariant martensitic phase transformations at large strains is formulated. The finite-element approach and an algorithm for the solution of corresponding problems are developed and implemented in a code FIDESYS. Cubic to tetragonal phase transformation in NiAl is studied. Various problems on stress-induced nucleation and evolution of martensitic variants in nanosize samples are solved, including a rectangular sample with single and multiple circular or elliptical nanovoids (with and without surface tension), as well as nanotube and beam. Importance of finite strain formulation is demonstrated. In particular, for the case when structural instability (buckling) of a beam is caused by phase transformation, for a geometrically linear formulation, phase transformation is suppressed. This is because finite rotation increases the energy of the system, while in a geometrically nonlinear theory energy is independent of rotation. Similar phase field and numerical approaches can be applied for twinning, dislocations, and reconstructive transformations.

© 2013 Elsevier Ltd. All rights reserved.

1. Introduction

Martensitic phase transformations are widely spread in modern material technologies and nature. They are responsible, in particular, for nontrivial thermomechanical effects in shape memory alloys; such as pseudoelasticity, pseudoplasticity, and shape memory effects. These effects are related to transformation of crystal lattice of austenite into crystal lattice of martensite. Due to symmetry of crystal lattice, several crystallographically equivalent and symmetry-related martensitic variants appear and can transform to each other. In order to simulate nucleation and evolution of multiple martensitic variants at the nanoscale under action of thermomechanical loading, Ginzburg–Landau or phase-field approaches are usually applied (Jin et al., 2001; Chen, 2002; Seol et al., 2002, 2003; Rasmussen et al., 2001; Idesman et al., 2008; Reid et al., 1998; Jacobs et al., 2003; Levitas et al., 2010; Levitas and Javanbakht, 2011b). The main computational advantage of the phase field approach is related to the fact that it does not require any additional efforts to track multiple and multi-connected interfaces. This is in contrast to traditional sharp interface approach (Levitas et al., 1998; Idesman et al., 2000), in which evolution is determined by sophisticated extremum principle or interface motion. In the phase field approach, the finite-width phase interfaces and their evolution are determined as a result of

the solution of a system of Ginzburg–Landau equations for n order parameters η_i , each of them describes evolution of the i th martensitic variant. This becomes possible under the choice of proper thermodynamic potential, which should have minima corresponding to austenite and martensitic variants. Since thermodynamic potential depends on the elastic strain (or stress) tensor, temperature, and order parameters, Ginzburg–Landau equations should be coupled to mechanical and thermal conduction equations. We will limit ourselves to an isothermal approximation in this paper.

There are two main choices of the order parameters for the martensitic phase transformations. In Refs. Jin et al. (2001), Wang and Khachaturyan (1997), Artemev et al. (2001), Seol et al. (2002, 2003), Levitas and Preston (2002a,b) and Levitas et al. (2003), the free energy is expressed in terms of transformation strain-related order parameters. In Refs. Rasmussen et al. (2001), Reid et al. (1998), Jacobs et al. (2003), Barsch and Krumhansl (1984) and Vedantam and Abeyaratne (2005), the order parameters are some components of the strain tensor. Some of the theories that are in terms of the total strain (Jacobs et al., 2003; Barsch and Krumhansl, 1984; Vedantam and Abeyaratne, 2005) utilize Lagrangian strain, i.e., they are applicable for large strains. There are, however, some drawbacks to this approach (Levitas and Preston, 2005; Levitas, 2013a). Some conditions that the potential should satisfy include the ability to describe the typical stress–strain curves observed experimentally and to include all of the temperature-dependent thermomechanical properties of austenite and martensitic variants; they are formulated in Levitas and Preston (2002a,b) and

* Corresponding author. Tel.: +1 (515) 294 9691; fax: +1 (801) 788 0026.

E-mail address: vlevitas@iastate.edu (V.I. Levitas).

Levitas et al. (2003). In particular, they are based on the consideration of instability conditions that results in the austenite–martensite and martensite–martensite transformation conditions. In contrast to the previous approaches, the advanced thermodynamic potentials developed in Levitas and Preston (2002a,b) and Levitas et al. (2003) in terms of the transformation strain-related order parameters satisfy these conditions for phase transformations between austenite and martensitic variants and between martensitic variants with arbitrary types of symmetry. We failed in trying to satisfy the same conditions and to include all of the temperature-dependent thermomechanical properties of austenite and martensitic variants when the total strain-related order parameters had been used. That is why all our further efforts have been focused on the transformation strain-related order parameters and we will not discuss strain related order parameters below.

Before our paper Levitas et al. (2009), all phase field simulations utilizing transformation strain-related order parameters were based on small strain theory. Later, theory by Levitas et al. (2009) was adjusted to large-strain treatment of twinning (Clayton and Knap, 2011a,b). At the same time, components of transformation strains for a shape memory alloy can exceed 0.2 and for phase transformations of graphite to diamond, hexagonal to cubic boron nitride, and from phase I to II in Si, Ge, and GaSb are of the order of magnitude of 0.5 (Britun and Kurdyumov, 2000; Malyushitskaya, 1999; Levitas, 2013a). Elastic strains can also be finite due to high pressure, lack of plastic relaxation in defect-free nanovolumes (in nanoparticles, nanowires, nanotubes, and nanofilms), and soft matter. For twinning in f.c.c. and b.c.c. crystals, transformation shear is as large as 0.71. Under some loading and conditions (for example, buckling), finite material rotations take place even at small strains but finite displacements. Large shears are always accompanied by large rotations. The importance of fully geometrically nonlinear formulations is well recognized in sharp-interface approaches (Bhattacharya, 2003; Pitteri and Zanzotto, 2002; Aubry et al., 2003; Ball and James, 1992; Grinfeld, 1991; Levitas, 2002; Idesman et al., 2000; Levitas and Ozsoy, 2009a,b).

Here, we utilize a fully geometrically nonlinear phase field theory for martensitic transformation developed in Levitas et al. (2009) and Levitas (2013a) for numerical simulation of martensitic transformations.

Most computational approaches to phase field equations are based on spectral methods (Jin et al., 2001; Wang and Khachaturyan, 1997; Artemev et al., 2001; Jacobs et al., 2003; Lookman et al., 2008; Saxena et al., 1997; Rasmussen et al., 2001). Khachaturyan et al. (Jin et al., 2001; Wang and Khachaturyan, 1997; Artemev et al., 2001; Chen, 2002) pioneered the approach, in which the spectral method is combined with an analytical Fourier-series solution to the elasticity equations for an arbitrary distribution of the order parameters, i.e., transformation strains, which makes numerical realization especially effective. However, such an approach is applicable to geometrically and physically linear problems only; and mostly to the periodic boundary conditions. Since theory developed in Levitas et al. (2009) and Levitas (2013a) contains multiple physical nonlinearities (the nonlinear elasticity law and nonlinear Ginzburg–Landau equations for η_i) and geometrical nonlinearities (finite strains and rotations, nonlinear multiplicative decomposition, and the change in geometry), the traditional spectral method cannot be used. Also, we would like to treat a finite size sample with holes, i.e., nonperiodic boundary conditions have to be applied. That is why in this paper we use finite element method (FEM). Because the thermodynamic potential has multiple minima corresponding to each phase, multiple stationary solutions are possible. Also, the solution strongly varies on the scale of the interface width and may oscillate in space due to a finely twinned martensite structure. Thus, special attention must be paid with regard to accuracy and convergence of the numerical solution. The

FEM solution for multivariant martensitic microstructure based on a small-strain version of our theory can be found in Levitas and Lee (2007), Levitas et al. (2010), Idesman et al. (2008), Cho et al. (2012), Levitas and Javanbakht (2011b), Levitas et al. (2010) and Levitas and Javanbakht (2010, 2011a), including dynamic 3D solutions. Here we present a computational approach and numerous examples for large-strain formulation suggested in Levitas et al. (2009) and Levitas (2013a). We will essentially utilize the methods developed in Levin (1998), Levin and Zingerman (1998) and Levin (1999) for viscoelastic materials and extend them to materials with phase transformations.

The paper is organized as follows. In Section 2, a complete system of coupled phase field and mechanical equations is presented based on the theory developed in Levitas et al. (2009) and Levitas (2013a). All material parameters are given for cubic to tetragonal phase transformation in NiAl. In Section 3, a numerical approach for large strains and for finite element discretization is presented. In Section 4, the results of numerous problems on stress-induced nucleation and evolution of martensitic variants in nanosize samples are solved and analyzed. In particular, problems on phase transformations in a rectangular sample with single and multiple circular or elliptical nanovoids (with and without surface tension), as well as in a nanotube and a beam are treated. The importance of finite strain formulation is demonstrated. Concluding remarks are given in Section 5. Some examples of the solution of finite-strain problems (none of which is presented here) without presenting algorithms have been reported in the short letter (Levitas et al., 2009).

Vectors and tensors are designated with boldface symbols; contractions of tensors $\mathbf{A} = \{A_{ij}\}$ and $\mathbf{B} = \{B_{ji}\}$ over one and two indices are designated as $\mathbf{A} \cdot \mathbf{B} = \{A_{ij}B_{jk}\}$ and $\mathbf{A} : \mathbf{B} = A_{ij}B_{ji}$, respectively. The transpose of \mathbf{A} is \mathbf{A}^T , and \mathbf{I} is the unit tensor; $:=$ means equal by definition; ∇ is the gradient operator with respect to undeformed configuration.

2. Coupled system of phase field and elasticity equations at finite strains

Here we will summarize and specify the main equations from Levitas et al. (2009) and Levitas (2013a). The total system of equations is presented in Box 1.

Kinematics and constitutive equations.

Let \mathbf{r}_0 and \mathbf{r} , be the positions of material points in the reference (undeformed) Ω_0 and the actual (final) Ω , configurations, respectively. Let the deformation of the elastic material with phase transformations be described by a vector function $\mathbf{r} = \mathbf{r}(\mathbf{r}_0, t)$, where t is the time. The material in the reference configuration is in the austenitic state. The deformation gradient $\mathbf{F} = \nabla \mathbf{r}$ is multiplicatively split into elastic \mathbf{F}_e and transformational \mathbf{U}_t contributions Eq. (1), where lattice rotation is included in \mathbf{F}_e , $\mathbf{U}_t = \mathbf{U}_t^T = \mathbf{I} + \boldsymbol{\varepsilon}_t$ is the symmetric tensor, and $\boldsymbol{\varepsilon}_t$ is the transformation strain. The transformation deformation gradient \mathbf{U}_t determines the locally unloaded (stress-free) configuration. For phase transformation between austenite A and i th martensitic variant M_i , the order parameter η_i is unambiguously related to the corresponding transformation strain $\boldsymbol{\varepsilon}_{ti}$; when the order parameter η_i varies between 0 for A and 1 for M_i , transformation strain varies between zero and $\boldsymbol{\varepsilon}_{ti}$. Introducing Lagrangian total \mathbf{E} , elastic \mathbf{E}_e , and transformational \mathbf{E}_t strain measures by Eqs. (2) and (3), one obtains with the help of Eq. (1) relationship Eq. (2) between them. The relationship between transformation deformation gradient \mathbf{U}_t and order parameters η_i is presented in Eq. (4) and depends on a parameter a .

The nonlinear elasticity law is presented in Eq. (5), where \mathbf{P} is the first nonsymmetric Piola–Kirchhoff (nominal) stress tensor (the force per unit area in the undeformed state), $\boldsymbol{\sigma}$ is the Cauchy (true) stress tensor (the force per unit area in the deformed state), $\hat{\boldsymbol{\sigma}}$ is the symmetric second Piola–Kirchhoff stress tensor with respect

to the unloaded configuration, ρ_0 , and ρ , are the mass density in the reference and deformed state, respectively, and ψ^e is the elastic part of the Helmholtz free energy, ψ , per unit undeformed volume. Elastic energy ψ^e is accepted in the form of Murnaghan elastic potential Eq. (6) (Lurie, 1990) that depends on three invariants of the tensor of elastic strain, E_m , see Eq. (7), and η_i -dependent elastic constants $C^{(j)}$ in Eq. (8). The expression for the local Helmholtz free energy ψ is given in Eq. (10). The change in thermal energy ΔG^0 and double well barrier A are defined in Eq. (11). In these equations, θ , is the temperature, θ_e , is the equilibrium temperature for stress-free A, and M, θ_c , is the critical temperature at which stress-free A, loses its thermodynamic stability; \bar{A} is the threshold for variant-variant transformation, similar to A for austenite–martensite transformation; B and D are parameters that do not affect the phase equilibrium or phase transformation conditions but affect thermodynamic potential at parameters η_i away from the A, and M_i , minima; and A_0 is the parameter. Kinetic Ginzburg–Landau Eqs. (12) and (13) for n order parameters contain the gradient energy coefficient β and the kinetic coefficient L . Equilibrium Eq. (14) are presented in undeformed configuration.

Box 1. Geometrically nonlinear problem formulation

1. Kinematics

Multiplicative decomposition of the deformation gradient \mathbf{F}

$$\mathbf{F} = \nabla \mathbf{r} = \mathbf{F}_e \cdot \mathbf{U}_t; \quad \mathbf{U}_t = \mathbf{U}_t^T. \quad (1)$$

Elastic strain tensor \mathbf{E}_e

$$\mathbf{E}_e := \frac{1}{2}(\mathbf{F}_{T_e} \cdot \mathbf{F}_e - \mathbf{I}) = \mathbf{U}_t^{-1} \cdot (\mathbf{E} - \mathbf{E}_t) \cdot \mathbf{U}_t^{-1}; \quad (2)$$

$$\mathbf{E} := \frac{1}{2}(\mathbf{F}^T \cdot \mathbf{F} - \mathbf{I}); \quad \mathbf{E}_t := \frac{1}{2}(\mathbf{U}_t \cdot \mathbf{U}_t - \mathbf{I}). \quad (3)$$

Transformation deformation gradient \mathbf{U}_t

$$\begin{aligned} \mathbf{U}_t &= \mathbf{I} + \boldsymbol{\varepsilon}_t = \mathbf{I} + \sum_{k=1}^n \boldsymbol{\varepsilon}_{tk} \varphi(a, \eta_k) \\ &\quad - \sum_{i=1}^{n-1} \sum_{j=i+1}^n \eta_i^2 \eta_j^2 (\eta_i \mathbf{L}_{ij} + \eta_j \mathbf{L}_{ji}), \\ \mathbf{L}_{ji} &= (a-3)\boldsymbol{\varepsilon}_{ji} + 3\boldsymbol{\varepsilon}_{ij}; \\ \varphi(a, \eta_i) &= a\eta_k^2(1-\eta_k)^2 + (4\eta_k^3 - 3\eta_k^4); \\ 0 < a < 6. \end{aligned} \quad (4)$$

2. Constitutive equations

Elasticity law for the first nonsymmetric Piola–Kirchhoff stress tensor \mathbf{P} , the Cauchy stress tensor $\boldsymbol{\sigma}$, and the second Piola–Kirchhoff stress tensor with respect to the unloaded configuration $\hat{\boldsymbol{\sigma}}$

$$\begin{aligned} \mathbf{P} &= \mathbf{F}_e \cdot \frac{\partial \psi^e}{\partial \mathbf{E}_e} \cdot \mathbf{F}_e^{-1}; \quad \boldsymbol{\sigma} = \frac{\rho}{\rho_0} \mathbf{F}_e \cdot \frac{\partial \psi^e}{\partial \mathbf{E}_e} \cdot \mathbf{F}_e^T; \\ \hat{\boldsymbol{\sigma}} &:= \frac{\rho_0}{\rho} \mathbf{F}_e^{-1} \cdot \boldsymbol{\sigma} \cdot \mathbf{F}_e^{T-1} = \mathbf{F}_e^{-1} \cdot \mathbf{P} \cdot \mathbf{F}_e^T = \frac{\partial \psi^e}{\partial \mathbf{E}_e}. \end{aligned} \quad (5)$$

Murnaghan elastic potential ψ^e

$$\begin{aligned} \psi^e(\mathbf{E}_e, C^{(k)}(\eta_1, \dots, \eta_n), \theta) \\ = 0.5C^{(1)}(\eta_1, \dots, \eta_n)(E_1)^2 + C^{(2)}(\eta_1, \dots, \eta_n)E_2 \\ + C^{(3)}(\eta_1, \dots, \eta_n)(E_1)^3 + C^{(4)}(\eta_1, \dots, \eta_n)E_1E_2 \\ + C^{(5)}(\eta_1, \dots, \eta_n)E_3, \end{aligned} \quad (6)$$

Invariants of the tensor of elastic strain E_m

$$\begin{aligned} E_1 &:= \mathbf{E}_e : \mathbf{I}; \quad E_2 := (\mathbf{E}_e \cdot \mathbf{E}_e) : \mathbf{I}; \\ E_3 &:= (\mathbf{E}_e \cdot \mathbf{E}_e \cdot \mathbf{E}_e) : \mathbf{I}. \end{aligned} \quad (7)$$

Elastic constants

$$\begin{aligned} C^{(j)}(\eta_1, \dots, \eta_n) &= C_0^{(j)} + \sum_{k=1}^n (C_k^{(j)} - C_0^{(j)})\phi(\eta_k), \\ j &= 1, 2, \dots, 5; \quad \phi(\eta_k) = \eta_k^2(3 - 2\eta_k). \end{aligned} \quad (8)$$

Local Helmholtz free energy

$$\begin{aligned} \psi(\mathbf{E}_e, \theta, \eta_i) &= \psi^e(\mathbf{E}_e, \theta, C^{(k)}(\eta_i)) + \sum_{k=1}^n f(\theta, \eta_k) \\ &\quad + \sum_{i=1}^{n-1} \sum_{j=i+1}^n \tilde{F}_{ij}(\eta_i, \eta_j); \end{aligned} \quad (9)$$

$$f(\theta, \eta_k) = A\eta_k^2(1 - \eta_k)^2 + \Delta G^0 \eta_k^3(4 - 3\eta_k);$$

$$\begin{aligned} \tilde{F}_{ij} &= \eta_i \eta_j (1 - \eta_i - \eta_j) [B((\eta_i - \eta_j)^2 - \eta_i - \eta_j) + D\eta_i \eta_j] \\ &\quad + (\bar{A} - A)\eta_i^2 \eta_j^2 (\eta_i + \eta_j) + \eta_i^2 \eta_j^2 (\eta_i K_i + \eta_j K_j); \end{aligned}$$

$$\begin{aligned} K_m &= 3\psi^e(\mathbf{E}_e, \theta, C_0^{(k)} - C_m^{(k)}) \\ &= 3 \left[0.5(C_0^{(1)} - C_m^{(1)})(E_1)^2 + (C_0^{(2)} - C_m^{(2)})E_2 \right. \\ &\quad + (C_0^{(3)} - C_m^{(3)})(E_1)^3 + (C_0^{(4)} - C_m^{(4)})E_1E_2 \\ &\quad \left. + (C_0^{(5)} - C_m^{(5)})E_3 \right], \quad m = i, j; \end{aligned} \quad (10)$$

Change in thermal energy ΔG^0 and double well barrier A

$$\Delta G^0 = A_0(\theta - \theta_e)/3, \quad A = A_0(\theta - \theta_c). \quad (11)$$

3. Ginzburg–Landau equations

$$\frac{1}{L} \dot{\eta}_i = \beta \nabla^2 \eta_i + X_i, \quad i = 1, \dots, n. \quad (12)$$

Local driving force for phase transformation

$$X_i := \mathbf{P}^T \cdot \mathbf{F}_e : \frac{\partial \mathbf{F}_t}{\partial \eta_i} - \frac{\partial \psi}{\partial \eta_i}, \quad i = 1, \dots, n. \quad (13)$$

4. Equilibrium equations in the undeformed configuration

$$\nabla \cdot \mathbf{P} = 0. \quad (14)$$

5. Boundary conditions for the order parameters

$$\mathbf{n} \cdot \nabla \eta_i = 0, \quad i = 1, \dots, n. \quad (15)$$

Boundary conditions Eqs. (15) for each order parameter correspond to the constant surface energy, which is independent of phase. For comparison, we will perform simulations for a simplified theory in which we take into account large displacement, but small strain and rotation formulation (Box 2). While we still distinguish between initial Ω_0 and deformed Ω , configurations and add finite displacements to the initial particles positions, the definition of the strain tensor \mathbf{E} (Eq. (16)) will be based on the geometrically linear theory and an additive decomposition of strain into elastic and transformational part will be used. The transformation strain tensor is defined as $\boldsymbol{\varepsilon}_t = \mathbf{U}_t - \mathbf{I}$ rather than $\boldsymbol{\varepsilon}_t = \mathbf{E}_t$. The elasticity rule for the Cauchy stress is given in Eq. (18). Gradient operators $\hat{\nabla}$ in the Ginzburg–Landau equations and boundary conditions are determined with respect to the deformed configuration. The gradient operators in Eq. (16) for strain and in equilibrium Eq. (25) are determined with respect to the initial configuration.

Box 2. Geometrically linear problem formulation

1. Kinematics

Additive decomposition of the strain tensor \mathbf{E}

$$\mathbf{E} = \frac{1}{2} [\mathbf{Vr} + (\mathbf{Vr})^T] = \mathbf{E}_e + \boldsymbol{\varepsilon}_t; \quad \boldsymbol{\varepsilon}_t = \boldsymbol{\varepsilon}_t^T. \quad (16)$$

Transformation strain tensor $\boldsymbol{\varepsilon}_t = \mathbf{U}_t - \mathbf{I}$

$$\begin{aligned} \boldsymbol{\varepsilon}_t &= \sum_{k=1}^n \boldsymbol{\varepsilon}_{tk} \varphi(a, \eta_k) - \sum_{i=1}^{n-1} \sum_{j=i+1}^n \eta_i^2 \eta_j^2 (\eta_i \mathbf{L}_{ij} + \eta_j \mathbf{L}_{ji}). \\ \mathbf{L}_{ji} &= (a-3)\boldsymbol{\varepsilon}_{ti} + 3\boldsymbol{\varepsilon}_{tj}; \quad \varphi(a, \eta_i) = a\eta_k^2(1-\eta_k)^2 \\ &\quad + (4\eta_k^3 - 3\eta_k^4); \quad 0 < a < 6. \end{aligned} \quad (17)$$

2. Constitutive equations

Elasticity law for the stress tensor $\boldsymbol{\sigma}$

$$\boldsymbol{\sigma} = \frac{\partial \psi^e}{\partial \mathbf{E}_e}. \quad (18)$$

Two-constant elastic potential ψ^e

$$\begin{aligned} \psi^e(\mathbf{E}_e, C^{(k)}(\eta_1, \dots, \eta_n), \theta) \\ = 0.5C^{(1)}(\eta_1, \dots, \eta_n)(E_1)^2 + C^{(2)}(\eta_1, \dots, \eta_n)E_2, \end{aligned} \quad (19)$$

Elastic constants

$$\begin{aligned} C^{(j)}(\eta_1, \dots, \eta_n) &= C_0^{(j)} + \sum_{k=1}^n (C_k^{(j)} - C_0^{(j)})\phi(\eta_k), \\ j = 1, 2; \quad \phi(\eta_k) &= \eta_k^2(3 - 2\eta_k). \end{aligned} \quad (20)$$

Local Helmholtz free energy

$$\begin{aligned} \psi(\mathbf{E}_e, \theta, \eta_i) &= \psi^e(\mathbf{E}_e, \theta, C^{(k)}(\eta_i)) + \sum_{k=1}^n f(\theta, \eta_k) \\ &\quad + \sum_{i=1}^{n-1} \sum_{j=i+1}^n \tilde{F}_{ij}(\eta_i, \eta_j); \end{aligned} \quad (21)$$

$$\begin{aligned} f(\theta, \eta_k) &= A\eta_k^2(1-\eta_k)^2 + \Delta G^0 \eta_k^2(4-3\eta_k); \\ \tilde{F}_{ij} &= \eta_i \eta_j (1-\eta_i-\eta_j) [B((\eta_i-\eta_j)^2 - \eta_i - \eta_j) + D\eta_i \eta_j] \\ &\quad + (\bar{A}-A)\eta_i^2 \eta_j^2 (\eta_i + \eta_j) + \eta_i^2 \eta_j^2 (\eta_i K_i + \eta_j K_j); \\ K_m &= 3\psi^e(\mathbf{E}_e, \theta, C_0^{(k)} - C_m^{(k)}) \\ &= 3 \left[0.5(C_0^{(1)} - C_m^{(1)})(E_1)^2 + (C_0^{(2)} - C_m^{(2)})E_2 \right], \\ m &= i, j. \end{aligned} \quad (22)$$

Change in thermal energy ΔG^0 and double well barrier A

$$\Delta G^0 = A_0(\theta - \theta_e)/3, \quad A = A_0(\theta - \theta_e). \quad (23)$$

3. Ginzburg–Landau equations

$$\frac{1}{L} \hat{\nabla}^2 \eta_i + \boldsymbol{\sigma} : \frac{\partial \boldsymbol{\varepsilon}_t}{\partial \eta_i} - \frac{\partial \psi}{\partial \eta_i}, \quad i = 1, \dots, n. \quad (24)$$

4. Equilibrium equations

$$\nabla \cdot \boldsymbol{\sigma} = 0. \quad (25)$$

5. Boundary conditions for the order parameters

$$\mathbf{n} \cdot \hat{\nabla} \eta_i = 0, \quad i = 1, \dots, n. \quad (26)$$

Material parameters. The following material parameters for cubic to tetragonal phase transformation in NiAl, determined and/or collected in Levitas and Preston (2002b), Levitas et al. (2003, 2010) and Rubini and Ballone (1993) will be used

$$\begin{aligned} A_0 &= 4.40 \text{ MPa K}^{-1}, \quad \beta = 2.59 \times 10^{-10} \text{ N}, \quad \theta_e = 215 \text{ K}, \\ \theta_c &= -183 \text{ K}, \quad \bar{A} = 5.32 \text{ GPa}, \\ a &= 2.98 \quad B = 0, \quad D = 5.5 \text{ GPa}, \quad L = 2600 \text{ (Pa} \cdot \text{s)}^{-1}. \end{aligned} \quad (27)$$

For our 2D FEM simulations we consider just two of the three possible NiAl martensitic variants

$$\begin{aligned} \boldsymbol{\varepsilon}_{t1} &= (0.215; -0.078; -0.078), \\ \boldsymbol{\varepsilon}_{t2} &= (-0.078; 0.215; -0.078), \end{aligned} \quad (28)$$

see Levitas and Preston (2005) and Levitas (2013a). Elastic constants in the potential Eqs. (6),

$$\begin{aligned} C_0^{(1)} &= 144 \text{ GPa}, \quad C_0^{(2)} = 74 \text{ GPa}, \\ C_1^{(1)} = C_2^{(1)} &= 379 \text{ GPa}, \quad C_1^{(2)} = C_2^{(2)} = 134 \text{ GPa}, \end{aligned} \quad (29)$$

were calculated as the orientational average of anisotropic moduli taken from Clapp et al. (1994) and Levitas and Preston (2002b); all other $C_i^{(j)} = 0$. Calculations have been performed at temperature $\theta = 0$.

Note that $\beta = 2.59 \times 10^{-10} \text{ N}$, corresponds to the width of an equilibrium interface $\delta \sim \sqrt{\beta/A} = 1 \text{ nm}$, for a M–M, interface (Levitas et al., 2003). We will introduce characteristic time $T \sim 1/(A\lambda) \simeq 0.5 \text{ ps}$ and characteristic stress for A–M PT under hydrostatic tension will be evaluated (with elastic strain neglected) as $\sigma = A/(a(\det \mathbf{F}_t - 1)) = 8.1 \text{ GPa}$ (Levitas and Preston, 2005). All size, time, and stress parameters will be normalized by $\delta = 1 \text{ nm}$, $T = 0.5 \text{ ps}$, and $\sigma_t = 10 \text{ GPa}$, respectively.

3. Numerical procedure

Because the free energy and transformation deformation gradient have multiple minima, multiple stationary solutions may be obtained. The solutions strongly vary on the scale of the interface width δ and may oscillate in space. Special attention has to be taken with respect to the accuracy of numerical solution. Numerical implementation for the coupled system of Eqs. (1)–(15) is performed for plane strain and plane stress problems. The solution is performed in the undeformed configuration with subsequent mapping of all the field into the deformed configuration. The primary unknowns are the order parameters η_i and displacements $\mathbf{u} := \mathbf{r} - \mathbf{r}_0$. In the Ginzburg–Landau Eq. (12) for the order parameters, the time derivative is substituted by its finite difference approximation

$$\frac{\partial \eta_i}{\partial t}(t_j) = \frac{\eta_i(t_j) - \eta_i(t_{j-1})}{\tau} + O(\tau), \quad (30)$$

where τ is the time step and $t_j = j\tau$. Then the time discretized Eq. (12) takes the form

$$\frac{\eta_i(t_j) - \eta_i(t_{j-1})}{\tau} = L\beta \nabla^2 \eta_k(t_j) + LX_i(t_j) + O(\tau). \quad (31)$$

These equations for the j th time step can be solved using the FEM (Zienkiewicz and Taylor, 2000a,b), if $\eta_i(t_{j-1})$ ($i = 1, \dots, n$) are known. After this, substituting found $\eta_i(t_j)$ in Eq. (4) for transformation strain, then determining elastic strains Eq. (2), stresses Eq. (5), and substituting them in the weak form of the equilibrium Equations. (14), displacements \mathbf{u} can be found at time t_j . Then the same procedure is repeated for the next time step.

Since the driving force $X_i(t_j)$ in Eq. (31) is unknown (because it depends on displacement at time t_j), the iteration predictor–cor-

rector procedure is used. Initially, the right-hand side in Eq. (31) is evaluated at time t_{j-1} , i.e. the following equation is solved

$$\frac{\eta_i(t_j) - \eta_i(t_{j-1})}{\tau} = L\beta\nabla^2\eta_k(t_{j-1}) + LX_k(t_{j-1}). \quad (32)$$

Then the above procedure to determine displacement field $u(t_j)$ from the solution of the system of equations of the elasticity problem with the determined $\eta_i(t_j)$ is performed. After this, the right-hand side of Eq. (31) is updated and the procedure is repeated. After finding all unknowns at time t_j , the same procedure is repeated for the next time instant. Linear triangle finite elements are used. The equilibrium equations result in a system of nonlinear algebraic equations with respect to displacements at nodes. It is solved with the help of Newton–Kantorovich methods, in which at each iteration a system of linear algebraic equations with a sparse matrix is solved.

Box 3. Numerical algorithm

1. Solution of nonlinear elastic problem (1)–(10), (14) for the finite body for a given distribution of the order parameters and determination of the displacement field \mathbf{u} at the initial time instant $t = 0$.
2. Solution of the Ginzburg–Landau Eq. (32) (starting with $j = 1$) using explicit finite difference scheme (predictor) and finding $\eta_i(t_j), i = 1, \dots, n$.
3. Solution of nonlinear elastic problem (1)–(10), (14) for the time instant t_j .
4. Updating solution $\eta_i(t_j)$ ($i = 1, \dots, n$) for the Ginzburg–Landau equation using implicit finite difference scheme (31) (corrector).
5. Solution of nonlinear elastic problem (1)–(10), (14) for the time instant t_j using updated $\eta_i(t_j)$ ($i = 1, \dots, n$).
6. If $\max_i \max_{V_0} |\eta_i(t_j) - \eta_i(t_{j-1})| \leq \varepsilon$ in the region V_0 for the small chosen ε , then the stationary solution is found. Otherwise, for the next time step $t_{j+1} = t_j + \tau, j \rightarrow j + 1$ move to the step 2.

The models and algorithms are implemented in the FEM code FIDESYS (FIDESYS, 2013) for the solution of corresponding coupled phase-field and elasticity problems. To verify accuracy of the

solution, several homogeneous (i.e., independent of position) problems have been solved using FIDESYS and Maple (Maple, 2013) codes. The difference in the order parameter and Cauchy stress components did not exceed 2%.

4. Results of simulations

Plane strain problems are considered. All results are presented in the deformed configuration. Color legends for the order parameters in all figures, which do not include them, are the same as in Fig. 1. The stationary state was considered to be reached if (1) the maximum increment of each order parameter over the all finite element nodes at the given time step did not exceed 0.005, or if (2) number of nodes in which this condition is violated did not exceed 1% of the total number of nodes. For some problems, even for stationary solution transformation cannot be completed (i.e., neither η_1 nor η_2 reached 1), which is related to the presence of a plane-strain constraint.

Solid samples

Problem 1. A square solid sample (i.e., without holes) of size $l = 27$ was loaded with the normal Cauchy stresses $p_1 = -0.7$ and $p_2 = 0.7$, corresponding to pure shear. In the circle of a radius $r = 2$ at the center of a sample, initial conditions $\eta_1 = \eta_2 = 0.1$ (i.e., the mixed embryo of martensitic phases M_1 and M_2) have been accepted. In the rest of the sample, here and in all other problems (excluding Problem 8), the material initially was in the austenitic state A ($\eta_1 = \eta_2 = 0$). The time step was $\tau = 0.05$; the area of each element was smaller than 0.1.

Order parameter η_1 in this problem reached zero in the entire sample after the first step and did not change after. It is not surprising because applied load promotes extension in the vertical direction and contraction in the horizontal direction and suppresses the opposite deformation. In Fig. 1, evolution of the distribution of the order parameter η_2 is shown, both in geometrically linear (upper row) and nonlinear (lower row) formulations, with the last column corresponding to the stationary solution. There is an evident qualitative difference between geometrically linear and nonlinear solutions in terms of the number of bands and the spacing between them.

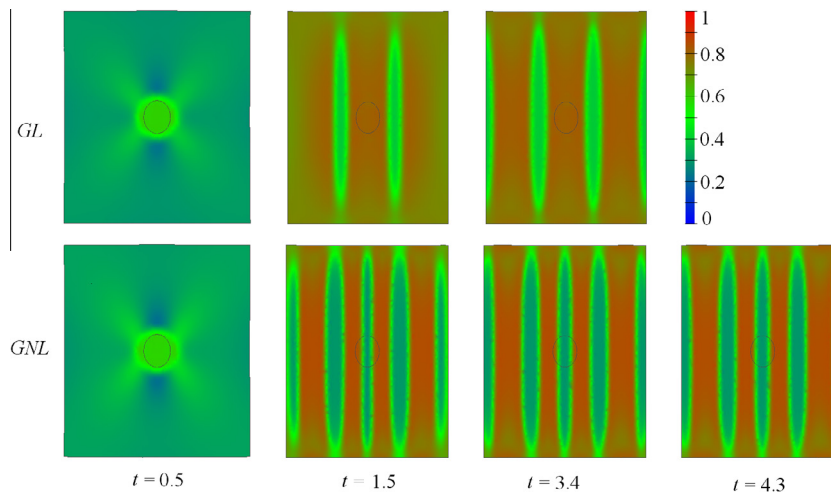


Fig. 1. Evolution of the distribution of the order parameter η_2 at different time instants (shown below the columns) for the Problem 1 for a square sample of the size $l = 27$ loaded with the normal Cauchy stresses $p_1 = -0.7$ and $p_2 = 0.7$. The upper row represents a geometrically linear (GL) solution, while a geometrically nonlinear (GNL) solution is shown in lower row. The last columns correspond to the stationary solution.

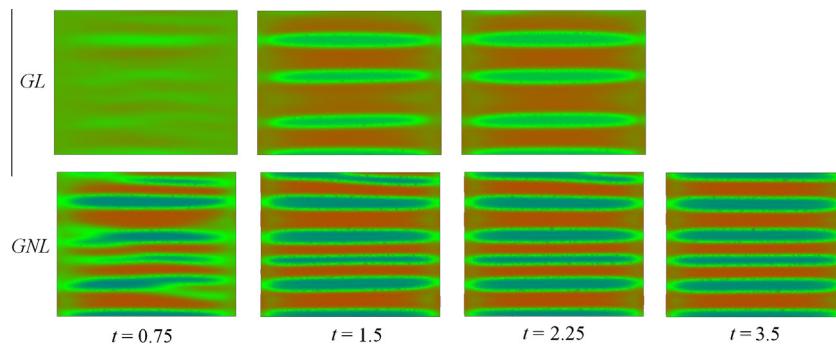


Fig. 2. Evolution of the distribution of the order parameter η_1 at different time instants (shown below the columns) for the Problem 2 for a square sample of the size $l = 26.6$ loaded with the normal Cauchy stress $p_1 = -1$ and $p_2 = 0$. Upper row represents geometrically linear (GL) solution, while geometrically nonlinear (GNL) solution is shown in the lower row. The last columns correspond to the stationary solution.

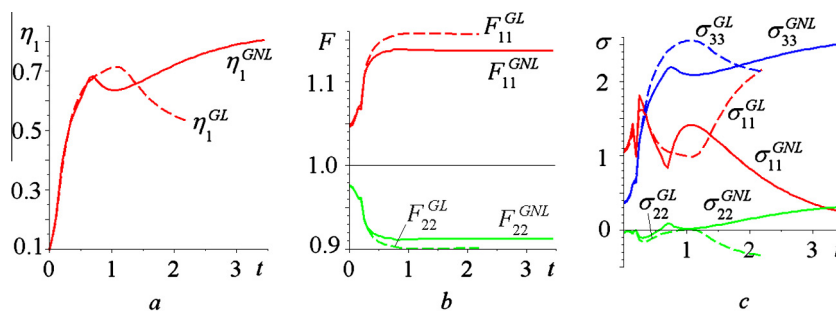


Fig. 3. Evolution of phase and stress-strain states in time at the central point $(0, 0)$ for the problem 2. (a) Order parameter η_1 ; (b) Components of deformation gradient tensor, red lines: F_{11} , green lines: $-F_{22}$; (c) Components of the Cauchy stress tensor, red line: σ_{11} , green line: σ_{22} , and blue line: σ_{33} . The solid lines are for the geometrically nonlinear (GNL) solution, while the dashed lines are for the geometrically linear (GL) solution. (For interpretation of the references to colour in this figure caption, the reader is referred to the web version of this article.)

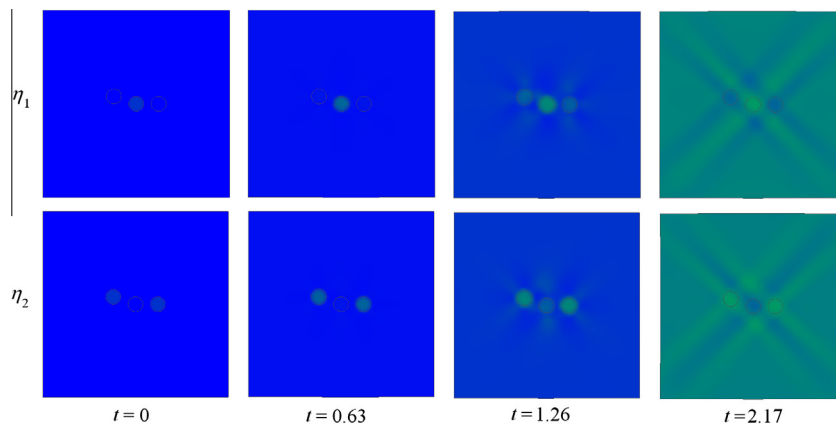


Fig. 4. Evolution of distribution of the order parameter η_1 (upper row) and η_2 (lower row) in a square sample of size $l = 82.3$ loaded with the normal Cauchy stresses $p_1 = p_2 = 1.5$ for Problem 3 in the geometrically nonlinear formulation. Time instants are shown below the columns. The last column corresponds to the stationary solution.

Problem 2. A square sample of size $l = 26.6$ was loaded with the normal Cauchy stress along the direction 1 $p_1 = 1$ and $p_2 = 0$. Initial values of the order parameters η_1 and η_2 represented stochastic numbers uniformly distributed between 0 and 1. The time step was $\tau = 0.05$; the area of each element was smaller than 0.09. Order parameter η_2 in this problem reached the stationary value equal to zero in the entire sample after the first step. In Fig. 2, evolution of the distribution of the order parameter η_1 is presented, both in geometrically linear (upper row) and nonlinear (lower row) formulations, with the last column corresponding to the stationary solution. Again, geometrically linear and nonlinear solutions differ qualitatively.

In Fig. 3, the evolution of the order parameter η_1 , components of the deformation gradient tensor, and the Cauchy stress tensor are presented. Significant differences between the geometrically linear and geometrically nonlinear solutions are clear.

Microstructures in Problems 1 and 2 are close to the periodic one. Note that even without stresses, a periodic solution exists but its energy is proportional to the number of units (Levitas et al., 2003). Still, it has the same stability as a single unit solution (Levitas et al., 2006a).

In the case of equiaxial tension $p_1 = p_2$ in the plane, stationary bands are directed under 45° with respect to axis 1. Again,

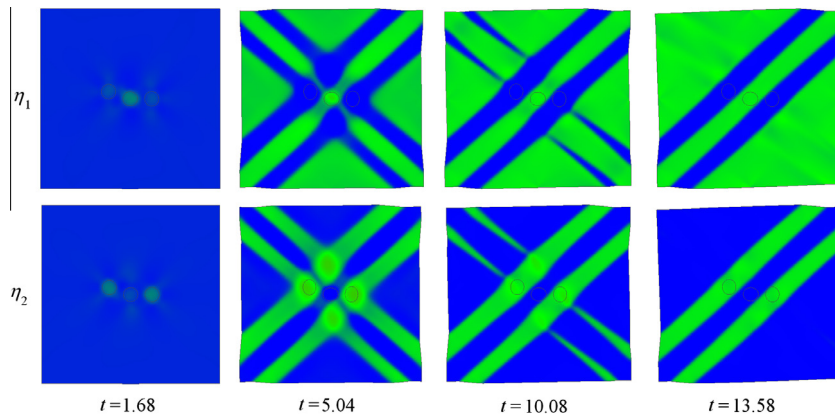


Fig. 5. Evolution of distribution of the order parameter η_1 (upper row) and η_2 (lower row) in a square sample of size $l = 82.3$ loaded with the normal Cauchy stresses $p_1 = p_2 = 1.5$ for Problem 3 in the geometrically linear formulation. Time instants are shown below the columns. The last column corresponds to the stationary solution.

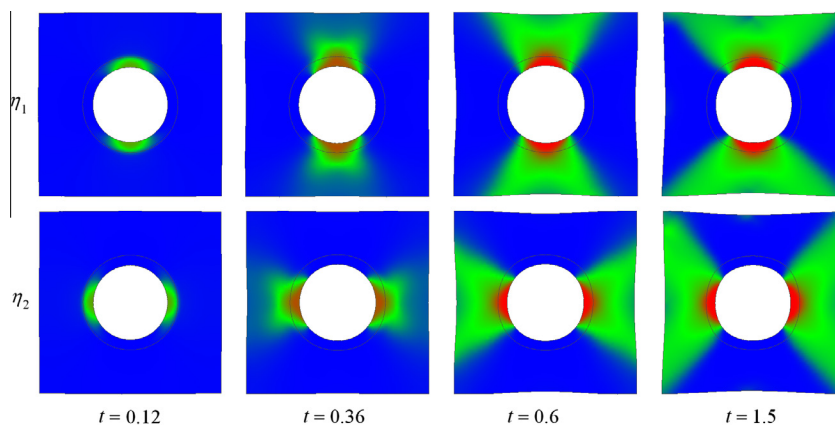


Fig. 6. Evolution of distribution of the order parameter η_1 (upper row) and η_2 (lower row) in a square sample of size $l = 26.6$ and circular central nanohole of a radius $r = 5$, was loaded with the normal Cauchy stresses $p_1 = p_2 = 1.5$ for Problem 4 in the geometrically nonlinear formulation. Time instants are shown below the columns. The last column corresponds to the stationary solution.

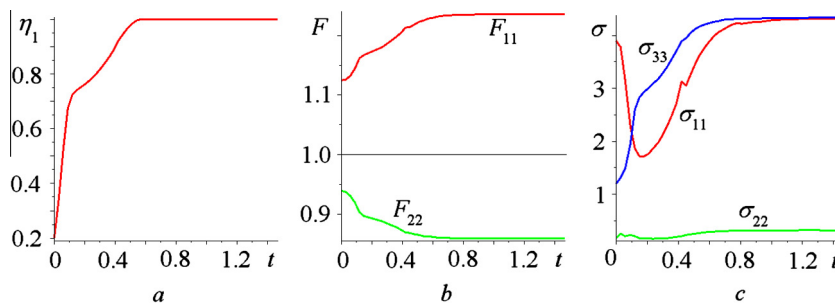


Fig. 7. Evolution of phase and stress–strain states in time at the central point $(0, 5.33)$ for problem 4. (a) Order parameter η_1 ; (b) Components of deformation gradient tensor, upper line: F_{11} , lower line: $-F_{22}$; (c) Components of the Cauchy stress tensor, red line: σ_{11} , green line: σ_{22} , and blue line: σ_{33} . (For interpretation of the references to colour in this figure caption, the reader is referred to the web version of this article.)

significant differences between the geometrically linear and geometrically nonlinear solutions are observed.

Problem 3. A square sample of size $l = 82.3$ was loaded with the normal Cauchy stresses $p_1 = p_2 = 1.5$. Three circular embryos of the radii 3.33 were prescribed as initial conditions: one of them at the center of a sample (point $(0; 0)$) had initially $\eta_1 = 0.1, \eta_2 = 0$, two others with the centers at the points $(-10; 3.33)$ and $(10; 0)$ possessed initially $\eta_1 = 0, \eta_2 = 0.1$. The rest of the sample was in the austenitic state. The time step was $\tau = 0.07$; the area of each element did not exceed 0.07. The geometrically nonlinear solution is presented in Fig. 4, while the geometrically linear solution is shown in Fig. 5. There is a drastic difference between the solutions.

The geometrically linear formulation promotes phase transformations and renders a more localized microstructure, which requires about six times larger time to reach the stationary solution. The solution with fourfold symmetry loses its stability and converges to the solution with twofold symmetry.

Sample with nanovoids

Problem 4. A square sample of size $l = 26.6$ and a circular central nanovoid of a radius $r = 5$, was loaded with the normal Cauchy stresses $p_1 = p_2 = 1.5$. Initial conditions $\eta_1 = 0.1, \eta_2 = 0.1$ (corresponding to the mixed M^1 and M^2 embryo) were prescribed in a ring with the internal boundary coinciding with the hole surface

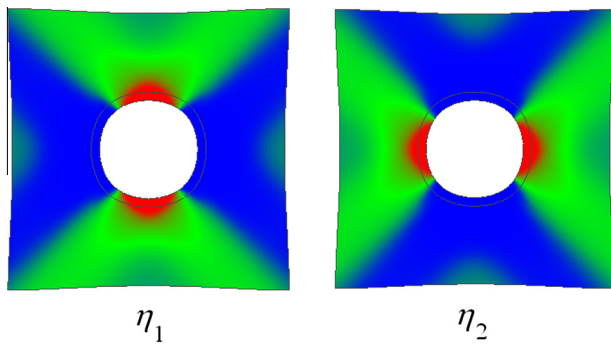


Fig. 8. Stationary solution for the order parameters for the sample of the size of 43.3, radius of the hole 6.66, external radius of the embryo 8.33, and stresses $p_1 = p_2 = 2$ (Problem 4a).

and the external radius of 6.67. The rest of a sample was in the austenitic state. The time step was $\tau = 0.03$; the area of each element did not exceed 0.06.

The geometrically nonlinear solution is presented in Fig. 6, in which the stationary state was reached at $t = 1.5$. Variant M_2 is located to the left and right of the hole, while variant M_1 is placed at the top and bottom of the hole. Both variants have approximately the same geometry and filled practically the entire sample. Bound-

aries between M_1 and M_2 are directed along the diagonals of a sample. Note that the distribution of the order parameter η_2 at any time instant coincides with the distribution of the order parameter η_1 rotated by 90° . Distribution of the order parameters is heterogeneous, reaching 1 close to the hole surface and 0.5 in the major part of the transformed region. In Fig. 7, the evolution of the order parameter η_1 , components of the deformation gradient, and the Cauchy stress at the point with coordinates $(0, 5.33)$ (origin of the coordinate system coincides with the hole center) is presented. The order parameter η_2 reached its stationary value equal to zero after the first time step. Due to symmetry, shear strains and stresses are absent at this point; thus, components in Fig. 7, b and c are the principle components of the deformation gradient and stress tensors.

For the same problem but with the larger load ($p_1 = p_2 = 2$), the results are qualitatively the same; however, the size of the regions, where the order parameters were close to 1, increased. The increase in size of the square to 33.3 with the same hole did not change results appreciably. Note that under equal compressive stresses, phase transformation is localized in small regions near the hole.

Problem 4a. For the same sample, but with the size of 43.3, radius of the nanovoid 6.66, external radius of the embryo 8.33, and stresses $p_1 = p_2 = 2$, results are shown in Fig. 8. They do not differ significantly from those of the previous sample.

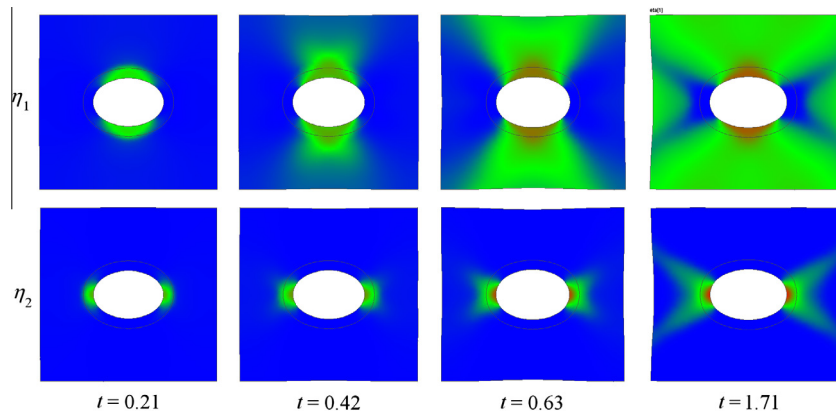


Fig. 9. Evolution of distribution of the order parameter η_1 (upper row) and η_2 (lower row) in a square sample of size $l = 26.6$, with a central elliptical nanovoid with semi-axes 5 and 3.33, loaded with the normal Cauchy stresses $p_1 = 1.2, p_2 = 0.9$ for Problem 5. Time instants are shown below the columns. The last column corresponds to the stationary solution.

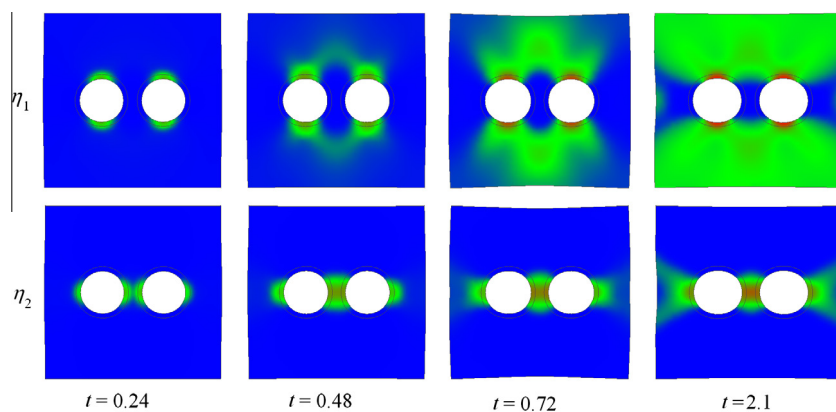


Fig. 10. Evolution of distribution of the order parameter η_1 (upper row) and η_2 (lower row) in a square sample with the size $l = 23.3$, two symmetric holes with $r = 2.66$ and distance between holes of 8, loaded by the tensile stress $p_1 = 1.2$ and $p_2 = 0.9$ for Problem 6. Time instants are shown below the columns. The last column corresponds to the stationary solution.

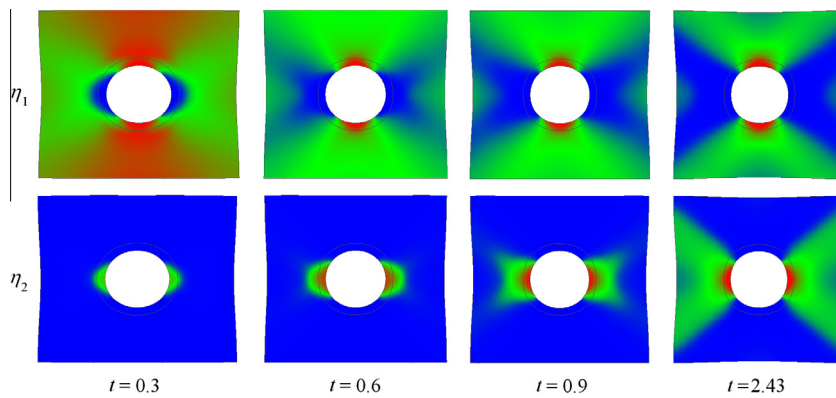


Fig. 11. Evolution of distribution of the order parameter η_1 (upper row) and η_2 (lower row) in a square sample of size $l = 26.6$ and circular central nanohole of a radius $r = 4$, which was loaded with the normal Cauchy stresses $p_1 = p_2 = 1.5$ for Problem 7. Time instants are shown below the columns. The last column corresponds to the stationary solution.

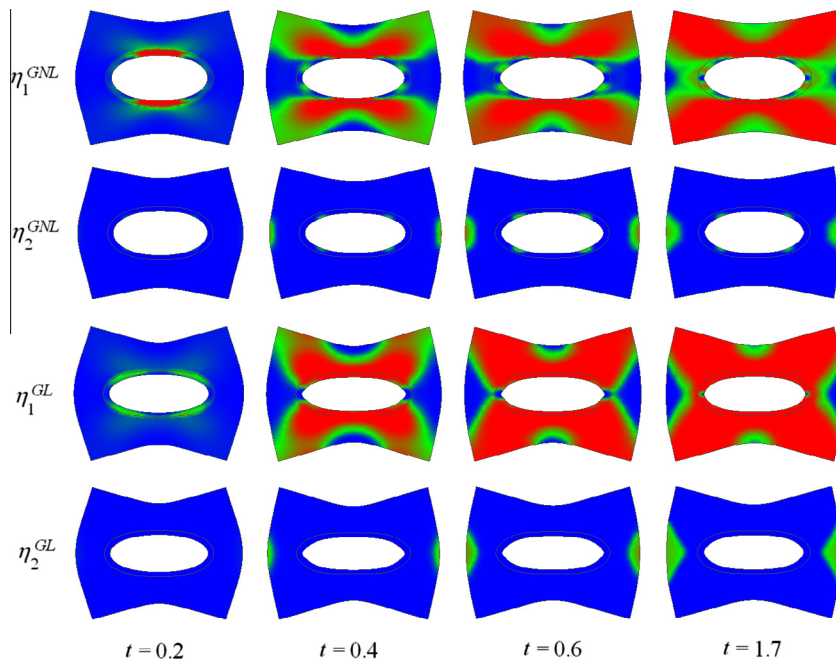


Fig. 12. Evolution of distribution of the order parameter η_1 (the first and third rows) and η_2 (the second and fourth rows) in a square sample of size $l = 25$, with a central circular nanovoid with radius $r = 6$, loaded with uniaxial normal Cauchy stress $p_1 = 2$ ($p_2 = 0$) for Problem 8. The first and second rows are for geometrically nonlinear solution, while the third and fourth rows are for geometrically linear formulation. Time instants are shown below the columns. The last column corresponds to the stationary solution.

Problem 5. A square sample of the size $l = 26.6$, with a central elliptical nanovoid with semiaxes 5 and 3.33 was loaded with the normal Cauchy stresses $p_1 = 1.2, p_2 = 0.9$. Initial conditions $\eta_1 = 0.1, \eta_2 = 0.1$ (corresponding to the mixed M_1 and M_2 embryo) were prescribed in a ring with the internal boundary coinciding with the nanovoid surface and the external ellipse with semiaxes 6.66 and 5. The rest of a sample was in the austenitic state. The time step and area of each element were similar to the previous problem. As it follows from Fig. 9, small portions of material at the left and right of the nanohole transformed to the variant M_2 , with the very small fully transformed region. The major part of the sample is transformed to the variant M_1 .

Problem 6. Results of simulations for a square sample with the size $l = 23.3$, two symmetric holes with $r = 2.66$ (located along axis 1) and a distance between holes of 8, loaded by the tensile Cauchy stress $p_1 = 1.2$ and $p_2 = 0.9$, are presented for three time instants in Fig. 10. The initial conditions $\eta_1 = \eta_2 = 0.1$ were pre-

scribed in rings of radius 3.33 around each hole. The time step was $\tau = 0.03$. Martensitic variant M_2 nucleates along the horizontal axis and covers region between the holes, with maximum $\eta_2 = 0.8$. Variant M_1 occupies the rest of the sample with complete transformation in a small regions above and below the holes.

Problem 7. A square sample of size $l = 26.6$ and circular central nanohole of a radius $r = 4$ was loaded with the normal Cauchy stresses $p_1 = p_2 = 1.5$. Initial conditions $\eta_1 = 0.9, \eta_2 = 0.1$ (corresponding to the M_2 embryo within M_1) were prescribed in a ring with the internal boundary coinciding with the hole surface and the external radius of 5.33. The rest of a sample was in the M_1 state, i.e., $\eta_1 = 1, \eta_2 = 0$. As can be seen in Fig. 11, initially the austenite appeared to the left and right of the hole, followed by transformation to the M_2 phase. In the stationary state, the M_1 - M_2 interfaces are directed under 45° and close to the diagonals of the square. The stationary state is close to that in the Problem 4 and is independent of the initial conditions.

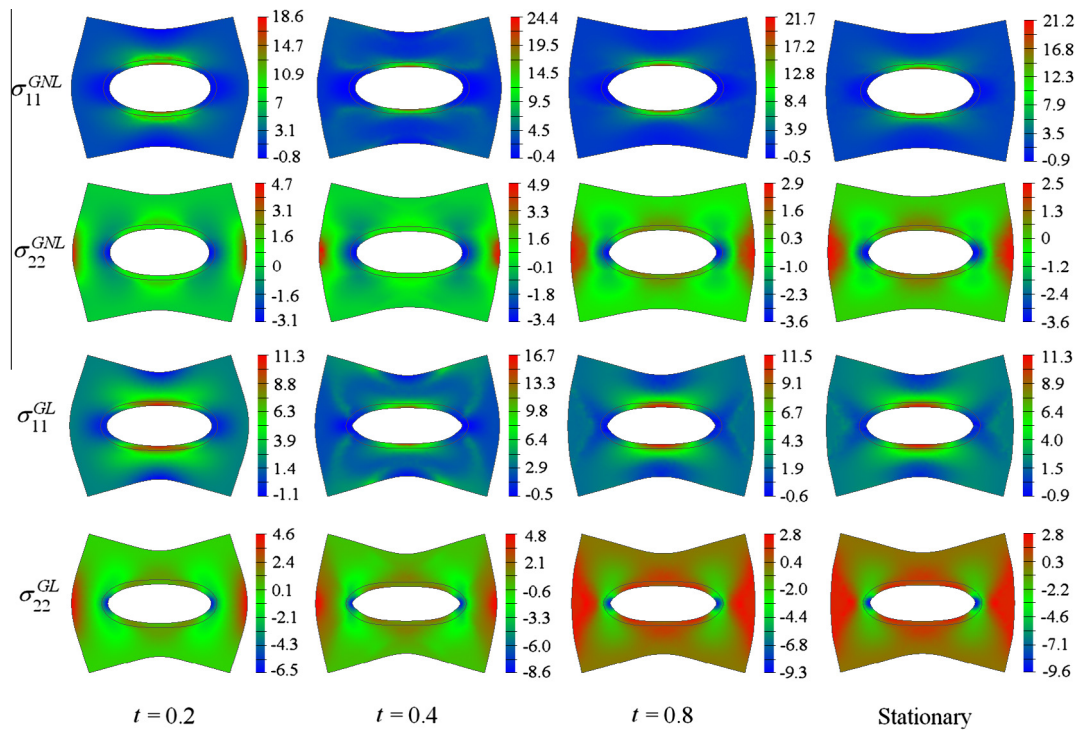


Fig. 13. Evolution of distribution of the Cauchy stresses σ_{11} (the first and third rows) and σ_{22} (the second and fourth rows) in a square sample of size $l = 25$, with a central circular nanovoid with radius $r = 6$, loaded with the uniaxial normal Cauchy stress $p_1 = 2$ ($p_2 = 0$) for Problem 8. The first and second rows are for the geometrically nonlinear solution, while the third and fourth rows are for the geometrically linear formulation. Time instants are shown below the columns. The last column corresponds to the stationary solution.

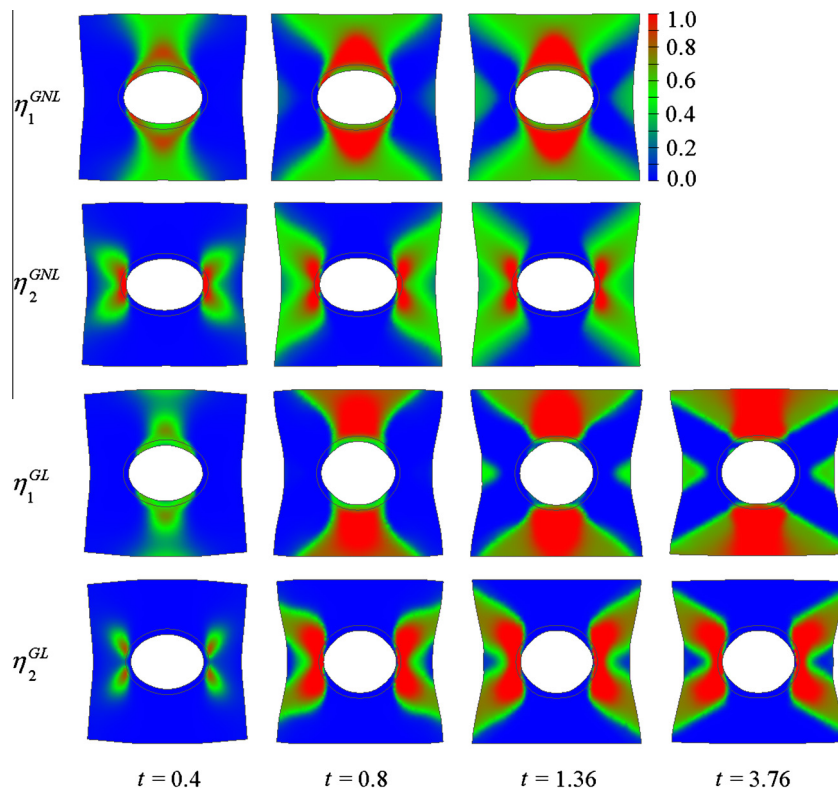


Fig. 14. Evolution of distribution of the order parameter η_1 (the first and third rows) and η_2 (the second and fourth rows) in a square sample of size $l = 25$, with a central elliptical nanovoid with semiaxes 6 and 2.5, loaded with the equiaxial normal Cauchy stress $p_1 = p_2 = 2.50$ for Problem 9. The first and second rows are for the geometrically nonlinear solution, while the third and fourth rows are for the geometrically linear formulation. Time instants are shown below the columns. The last columns correspond to the stationary solutions.

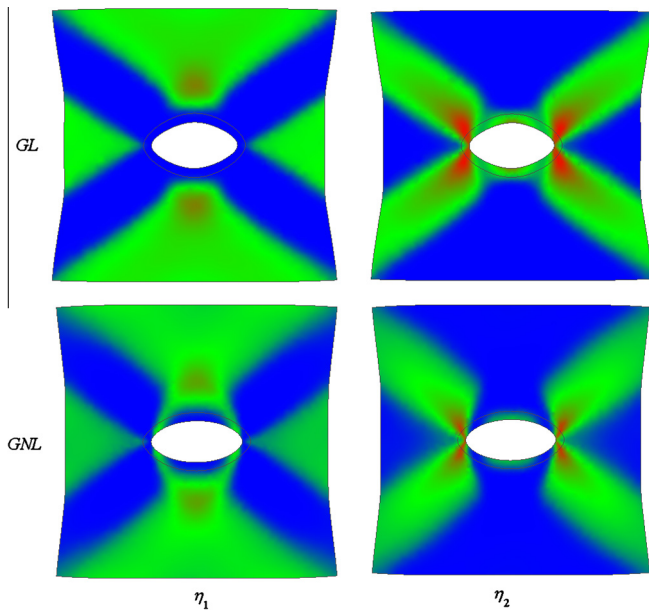


Fig. 15. Stationary distribution of the order parameter η_1 (the first column) and η_2 (the second column) in a square sample of the size $l = 8$, with a central elliptical nanovoid with semiaxes 1.5 and 0.3 for Problem 10. The sample loaded with the equiaxial normal Cauchy stress $p_1 = p_2 = 1.5$ and distributed normal to the hole in the deformed state stress due to surface tension equal to γk , with $\gamma = 8$ GPa/nm. The first row is for the geometrically linear formulation, while the second row is for the geometrically nonlinear formulation.

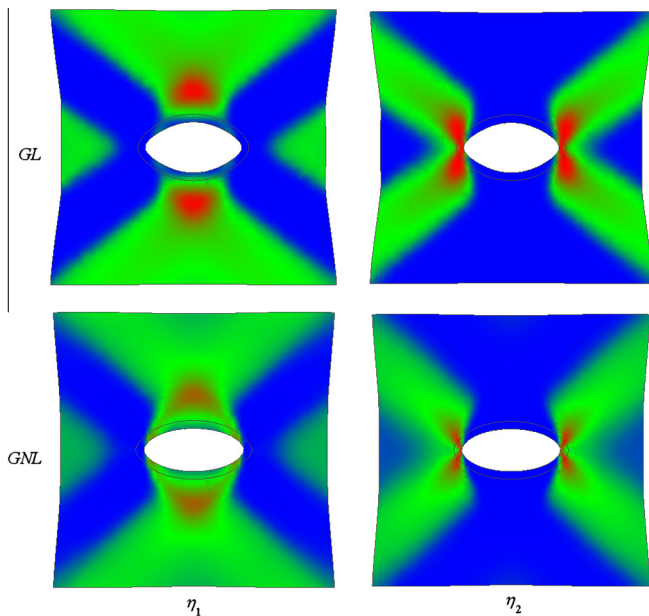


Fig. 16. The same solutions as in Fig. 15 without surface tension.

Problem 8. A square sample of the size $l = 25$, with a central circular nanovoid with radius $r = 6$ was loaded with the uniaxial normal Cauchy stress $p_1 = 2$ ($p_2 = 0$). Initial conditions $\eta_1 = 0.1$, $\eta_2 = 0.1$ were prescribed in a ring with the internal boundary coinciding with the nanovoid surface and the external circle with radius 7. The rest of a sample was in the austenitic state. As expected (see Fig. 12), the major part of the sample transforms to M_1 . Incomplete variant M_2 is found in a small regions near vertical (in the reference state) external surfaces along axis 1. Residual austenite is observed in a small regions near the hole along axis 1.

The geometrically nonlinear and linear solutions exhibit a large change in shape and are qualitatively close, however some differences exist. Thus, the geometrically nonlinear solution contains very small embryos of the variant M_2 near the hole, which are absent in geometrically linear solutions. Also, in geometrically linear solutions the region with the variant M_1 is slightly larger, as is the elongation of the hole in horizontal direction. At the same time, the distribution of the true normal stresses σ_{11} and σ_{22} (Fig. 13) differ essentially for the geometrically linear and nonlinear formulations. For the geometrically nonlinear solution, the maximum stress σ_{11} is almost 2 times larger than in the geometrically linear case. This result shows the importance of geometrically nonlinear formulation for the evaluation of fracture in the structural elements at the nanoscale during phase transformations.

Problem 9. A square sample of the size $l = 25$, with a central elliptical nanovoid with semiaxes 6 and 2.5 was loaded with the equiaxial normal Cauchy stresses $p_1 = p_2 = 2.5$. Initial conditions $\eta_1 = 0.1$, $\eta_2 = 0.1$ were prescribed in a ring with the internal boundary coinciding with the nanovoid surface and the external ellipse with semiaxes 7 and 3.5. The rest of a sample was in the austenitic state. Results are shown in Fig. 14 for both the geometrically nonlinear and linear solutions. For both formulations, the variant M_1 is located near the hole surface with smaller curvature, while the variant M_2 is placed near the hole surface with larger curvature. The region with fully transformed M_1 exceeds that with fully transformed M_2 . The shape of the hole changes significantly, especially for the geometrically linear solution. An ellipse with an aspect ratio more than 2 deforms toward the circle. The regions with fully transformed martensite are larger for the geometrically linear formulation, the same as time required to reach stationary states (1.88 and 0.68 for the geometrically linear and nonlinear solutions, respectively).

Effect of surface tension

In the next three problems, the component 3 of the transformation strain tensors ϵ_{ii} orthogonal to the plane of the figure is zero. The effect of the surface tension at the internal and external surfaces is taken into account in boundary conditions for stresses. Thus, distributed normal (to the internal and external surfaces in the deformed state) stress due to surface tension equal to γk (where γ is the surface energy and k is the local curvature) is applied. Since surface energy is assumed to be constant, it does not affect solution.

Problem 10. A square sample of the size $l = 8$, with a central elliptical nanovoid with semiaxes 1.5 and 0.3 was loaded with the equiaxial normal Cauchy stresses $p_1 = p_2 = 1.5$; $\gamma = 8$ GPa/nm. Initial conditions $\eta_1 = 0.1$, $\eta_2 = 0.1$ were prescribed in a ring with the internal boundary coinciding with the nanovoid surface and the external ellipse with semiaxes 1.75 and 0.55. The rest of a sample was in the austenitic state. Stationary distributions of the order parameters for geometrically nonlinear and linear formulations with and without surface tension are shown in Fig. 15. While qualitatively results for both formulations are similar, there are some essential differences. Thus, for the geometrically nonlinear formulation the variant M_1 touches the void surface, for the geometrically linear formulation it does not. Also, the shape of the final nanohole looks different. In Fig. 16, the same problem is solved without surface tension, for both formulations. With surface tension, the region above and below the hole is occupied by the variant M_2 ; without surface tension it is occupied by austenite. Also, surface tension reduces the size of the hole.

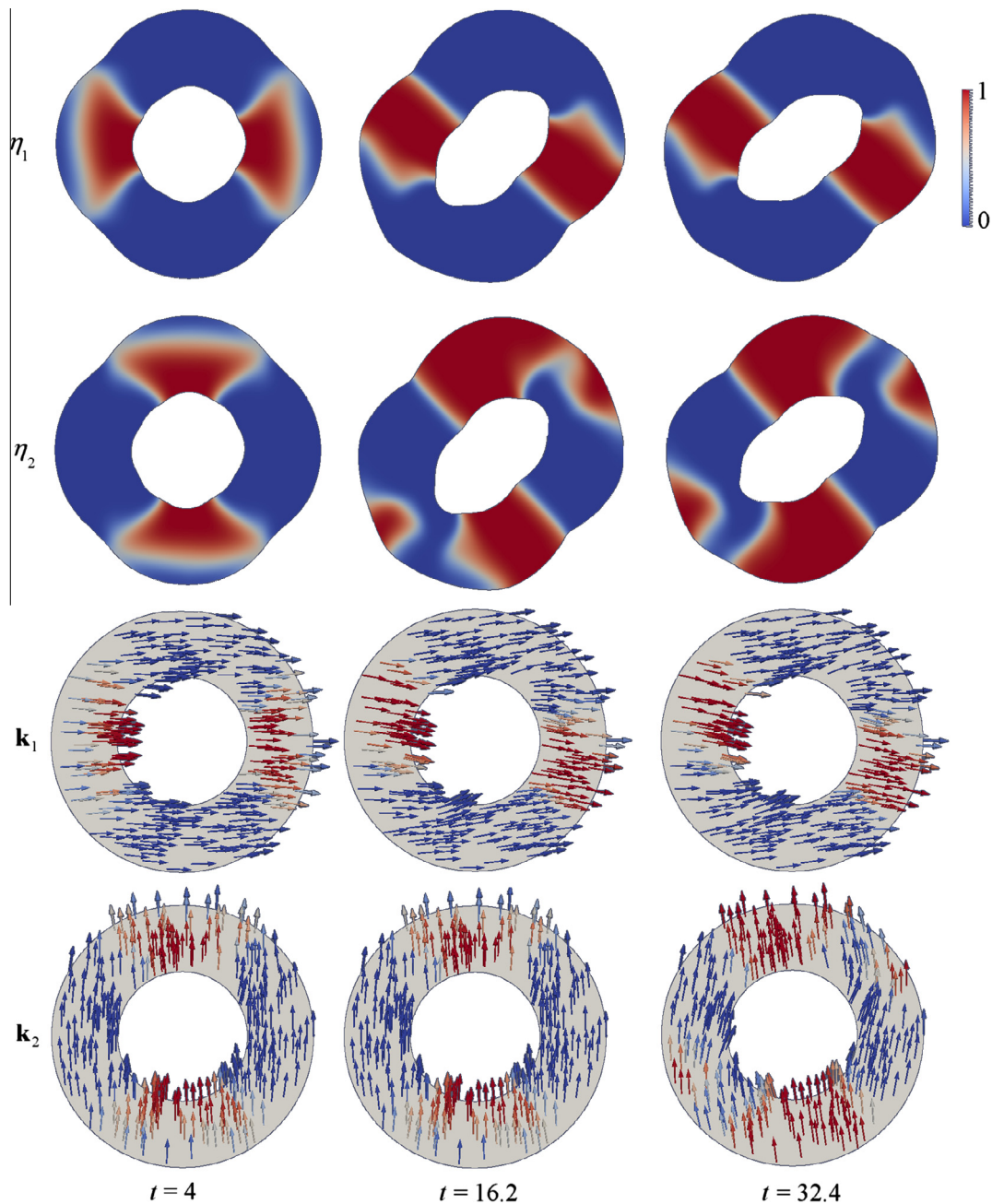


Fig. 17. Stationary distribution of the order parameter η_1 (the first row) and η_2 (the second row) in a nanotube with internal radius 1 and external radius 2 for Problem 11. The third and fourth rows show the evolution of orientation of vectors \mathbf{k}_1 and \mathbf{k}_2 , which were initially directed along the horizontal and vertical axes, respectively. The ring is loaded by distributed normal to the internal and external surfaces (in the deformed state) stress equal to γk , with $\gamma = 4$ GPa/nm. Geometrically nonlinear formulation. Time instants are shown below the columns. The last column corresponds to the stationary solutions.

Problem 11. Ring (i.e., nanotube) with internal radius 1 and external radius 2 is fixed at two external surface points, which are located at the vertical symmetry axis. One of these points is fixed rigidly, and for other point only horizontal displacement is possible. The ring is loaded by distributed normal to the deformed internal and external surfaces stress equal to γk , with $\gamma = 4$ GPa/nm. Initial conditions $\eta_1 = \eta_2 = 0.1$ were prescribed in a ring with the internal boundary coinciding with the hole surface and the external radius of 1.2. The rest of a sample was in the austenitic state. Stationary distributions of the order parameters for geometrically nonlinear and linear formulations are presented in Figs. 17 and 18, respectively. In addition, the evolution of orientation of vectors \mathbf{k}_1 and \mathbf{k}_2 , which were initially directed along the horizontal and

vertical axes, respectively, is shown in these figures. There is an evident difference between these two formulations. In particular, the linear solutions are nearly symmetric with respect to the reflection with respect to horizontal and vertical mirrors, but the geometrically nonlinear solution does not possess such a symmetry property. The final shape of the ring differs as well.

Effect of large rotations

Problem 12. A rectangular beam of sizes 10 and 1 and with a fixed left end is loaded by a compressive horizontal Cauchy stress of 1 and by a compressive vertical Cauchy stress of 0.005 (both in the

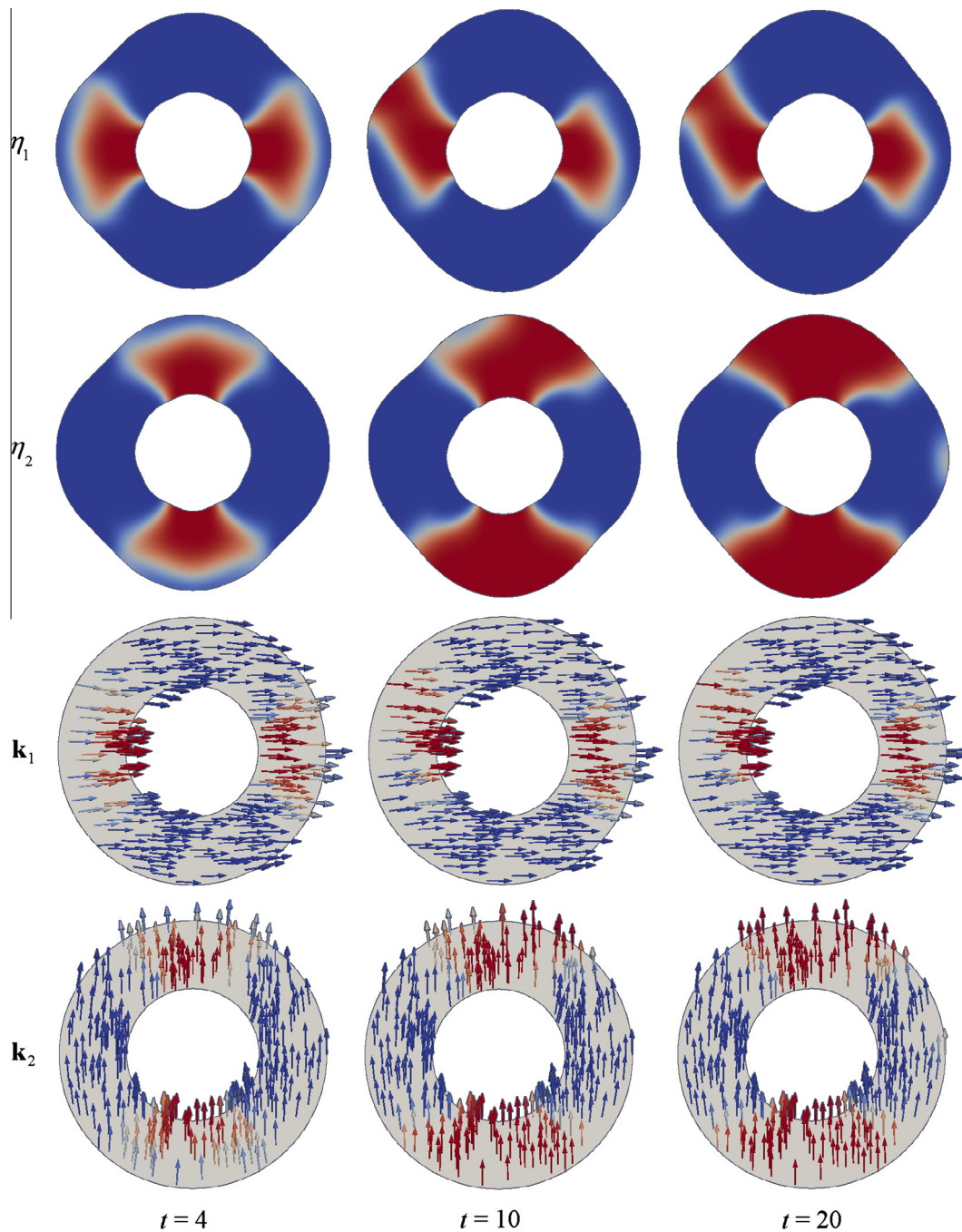


Fig. 18. The same solutions like in Fig. 17 but for geometrically linear formulation.

deformed state). Initial conditions $\eta_1 = \eta_2 = 0.1$ were prescribed in a ring shown in Fig. 19; the rest of a sample was in the austenitic state. The stationary solution for the geometrically linear problem represented a homogeneous austenitic state and plate remained rectangular. The stationary solution for the geometrically nonlinear problem is shown in Fig. 19 and demonstrates significant buckling, alternating M_1 and M_2 variants near the fixation and variant M_1 in the rest of the sample. Note that the variants M_1 (and M_2) in different regions differ by rigid-body rotations. Thus, structural instability (buckling) is caused by phase transformation. However, for the geometrically linear formulation, phase transformation is suppressed, because finite rotation increases the energy of the system, while in a strict geometrically nonlinear theory energy is independent of finite rotations.

5. Concluding remarks

To summarize, the numerical procedure for the simulation of multivariant stress-induced martensitic phase transformations for the most general case of large elastic and transformational strains and rotations, as well as for nonlinear and different elastic properties of phases, is developed. The models and algorithms are implemented in the FEM code FIDESYS for the solution of corresponding coupled phase-field and elasticity problems. Problems of martensitic variant nucleation and evolution in a nanosize sample with and without single and multiple circular and elliptic nanovoids are solved. The effect of surface tension and large rotations is studied as well. The qualitative difference between small strain and large-strain solutions is demonstrated. In particular,

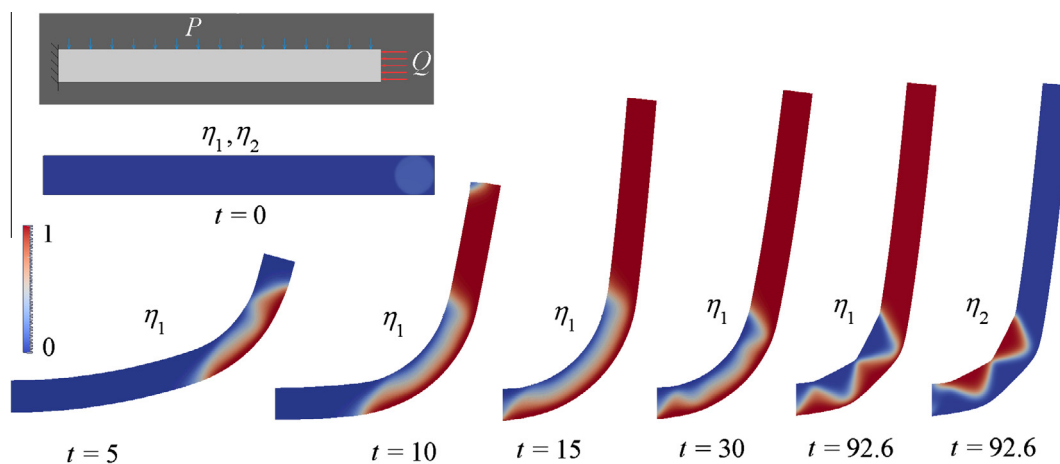


Fig. 19. Loading conditions, evolution of distribution of the order parameter η_1 , and stationary distribution of the order parameters η_1 and η_2 in a nanoplate of sizes 10 and 1 and with the fixed left end. Plate is loaded by compressive horizontal Cauchy stress of 1 and by compressive vertical Cauchy stress of 0.005 (both in the deformed state) in geometrically nonlinear formulation. The loading conditions and the initial distribution of the order parameters η_1 and η_2 are shown in the upper left corner: the loading conditions are in the first row, and the initial distribution of the order parameters is in the second one. Time instants are shown below the columns. The last two columns correspond to the stationary solutions of the order parameters.

for the case when structural instability (buckling) is caused by phase transformation, phase transformation is suppressed in the small strain setting. This is because finite rotation increases energy of the system, while in a strict geometrically nonlinear theory energy is independent of rotations. A similar computational framework can be applied for reconstructive phase transformations (when atoms change their neighbors), and transformations in soft matter (e.g., in polymers and biological materials), where strains are very large, as well as for twinning, dislocations (Levitas and Javanbakht, 2012), and fracture. Transformation shear strain induced by twinning and dislocation are large, as well as the transformation tensile strain (simulating bond breaking) and elastic strains near the crack tip. As the next step, our approach will be extended to dynamic problem formulations and applied to phase transformations in a shock wave. It will be also applied for the extension of our microscale phase field approach (Idesman et al., 2005; Levitas et al., 2004; Levitas and Ozsoy, 2009a; Levitas and Ozsoy, 2009b). It is worth to note that a finite strain formulation plays a key role for the introduction of surface tension in the phase field approach (Levitas and Javanbakht, 2010; Levitas and Samani, 2011a,b; Levitas and Javanbakht, 2011a; Levitas, 2013b; Levitas, 2013c).

Acknowledgements

The support of National Science Foundation (CMMI-0969143), Army Research Office (W911NF-12-1-0340), Defense Advanced Research Projects Agency (W31P4Q-13-1-0010), Office of Naval Research (N00014-12-1-0525), Iowa State University, and Los Alamos National Laboratory for VIL is gratefully acknowledged. Discussions and collaboration with Dr. Dean Preston (Los Alamos National Laboratory) are greatly appreciated. VAL, KMZ, and EIF acknowledge the support of NVIDIA Corporation, Russian Foundation for Basic Research (projects 11-01-12043-ofi-m-2011, 11-08-01284-a), Skolkovo Foundation, and the Ministry of Education and Science of Russian Federation (State contract No. 07.514.12.4021 for scientific research). KMZ and EIF acknowledge the financial support of the Ministry of Education and Science of Russian Federation (State contract No. 07.524.11.4019, funding from the Federal Targeted Program "Research and Development in Priority Fields of the Scientific and Technological Complex of Russia (2007–2013)").

References

- Artemev, A., Jin, Y., Khachatryan, A.G., 2001. Three-dimensional phase field model of proper martensitic transformation. *Acta Mater.* 49, 1165–1177.
- Aubry, S., Fago, M., Ortiz, M., 2003. A constrained sequential-lamination algorithm for the simulation of sub-grid microstructure in martensitic materials. *Comput. Methods Appl. Mech. Eng.* 192, 2823–2843.
- Ball, J., James, R.D., 1992. Proposed experimental tests of a theory of fine microstructure and the two-well problem. *Proc. R. Soc. London A Math. Phys. Sci.* 338, 389–450.
- Barsch, G.R., Krumhansl, J.A., 1984. Twin boundaries in ferroelastic media without interface dislocations. *Phys. Rev. Lett.* 53, 1069–1072.
- Bhattacharya, K., 2003. *Microstructure of martensite. Why it Forms and How It Gives Rise to the Shape-Memory Effect.* Oxford University Press, Oxford.
- Britun, V.F., Kurdyumov, A.V., 2000. Mechanisms of martensitic transformations in boron nitride and conditions of their development. *High Press. Res.* 17, 101–111.
- Chen, L.Q., 2002. Phase-field models for microstructure evolution. *Annu. Rev. Mater. Res.* 32, 113–140.
- Cho, J.-Y., Idesman, A.V., Levitas, V.I., Park, T., 2012. Finite element simulations of dynamics of multivariant martensitic phase transitions based on Ginzburg–Landau theory. *Int. J. Solids Struct.* 49, 1973–1992.
- Clayton, J.D., Knap, J., 2011a. A phase field model of deformation twinning: nonlinear theory and numerical simulations. *Phys. D* 240, 841–858.
- Clayton, J.D., Knap, J., 2011b. Phase field modeling of twinning in indentation of transparent crystals. *Model. Simul. Mater. Sci. Eng.* 19, 085005.
- Clapp, P.C., Besquart, C.S., Shao, Y., Zhao, Y., Rifkin, J.A., 1994. Transformation toughening explored via molecular dynamics and Monte Carlo simulations. *Model. Simul. Mater. Sci. Eng.* 2, 551–558.
- FIDESYS, 2013. <<http://www.cae-fidesys.com/>>
- Grinfeld, M.A., 1991. *Thermodynamic Methods in the Theory of Heterogeneous Systems.* Longman, Sussex.
- Idesman, A.V., Levitas, V.I., Stein, E., 2000. Structural changes in elastoplastic materials: a unified finite element approach for phase transformation, twinning and fracture. *Int. J. Plast.* 16, 893–949.
- Idesman, A.V., Levitas, V.I., Preston, D.L., Cho, J.-Y., 2005. Finite element simulations of martensitic phase transitions and microstructure based on strain softening model. *J. Mech. Phys. Solids* 53, 495–523.
- Idesman, A.V., Cho, J.-Y., Levitas, V.I., 2008. Finite element modeling of dynamics of martensitic phase transitions. *Appl. Phys. Lett.* 93, 043102.
- Jacobs, A.E., Curnoe, S.H., Desai, R.C., 2003. Simulations of cubic-tetragonal ferroelastics. *Phys. Rev. B* 68, 224104.
- Jin, Y.M., Artemev, A., Khachatryan, A.G., 2001. Three-dimensional phase field model of low-symmetry martensitic transformation in polycrystal: simulation of zeta (ζ) martensite in AuCd alloys. *Acta Mater.* 49, 2309.
- Levin, V.A., 1998. Theory of repeated superposition of large deformations. Elastic and viscoelastic bodies. *Int. J. Solids Struct.* 35, 2585–2600.
- Levin, V.A., 1999. *Multiple Superposition of Large Deformation in Elastic and Viscoelastic Bodies.* Nauka, Moscow (in Russian).
- Levin, V.A., Zingerman, K.M., 1998. Interaction and microfracturing pattern for successive origination (introduction) of pores in elastic bodies: finite deformation. *Trans. ASME. J. Appl. Mech.* 65, 431–435.
- Levitas, V.I., 2002. Critical thought experiment to choose the driving force for interface propagation in inelastic materials. *Int. J. Plast.* 18, 1499–1525.

- Levitas, V.I., 2013a. Phase-field theory for martensitic phase transformations at large strains. *Int. J. Plast.*. <http://dx.doi.org/10.1016/j.ijplas.2013.03.002>.
- Levitas, V.I., 2013b. Interface stresses for nonequilibrium microstructures in phase field approach: exact analytical results. *Phys. Rev. B* 87, 054112.
- Levitas, V.I., 2013c. Thermodynamically consistent phase field approach to phase transformations with interface stresses. *Acta Mater.* 61, 4305–4319.
- Levitas, V.I., Javanbakht, M., 2010. Surface tension and energy in multivariant martensitic transformations: phase-field theory, simulations, and model of coherent interface. *Phys. Rev. Lett.* 105, 165701.
- Levitas, V.I., Javanbakht, M., 2011a. Surface-induced phase transformations: multiple scale and mechanics effects and morphological transitions. *Phys. Rev. Lett.* 107, 175701.
- Levitas, V.I., Javanbakht, M., 2011b. Phase-field approach to martensitic phase transformations: effect of martensite–martensite interface energy. *Int. J. Mater. Res.* 102, 652–665.
- Levitas, V.I., Javanbakht, M., 2012. Advanced phase field approach to dislocation evolution. *Phys. Rev. B, Rapid Commun.* 86, 140101(R).
- Levitas, V.I., Lee, D.-W., 2007. Athermal resistance to an interface motion in phase field theory of microstructure evolution. *Phys. Rev. Lett.* 99, 245701.
- Levitas, V.I., Ozsoy, I.B., 2009a. Micromechanical modeling of stress-induced phase transformations. Part 1. Thermodynamics and kinetics of coupled interface propagation and reorientation. *Int. J. Plast.* 25, 239–280.
- Levitas, V.I., Ozsoy, I.B., 2009b. Micromechanical modeling of stress-induced phase transformations. Part 2. Computational algorithms and examples. *Int. J. Plast.* 25, 546–583.
- Levitas, V.I., Preston, D.L., 2002a. Three-dimensional Landau theory for multivariant stress-induced martensitic phase transformations. I. Austenite \leftrightarrow martensite. *Phys. Rev. B* 66, 134206.
- Levitas, V.I., Preston, D.L., 2002b. Three-dimensional Landau theory for multivariant stress-induced martensitic phase transformations. II. Multivariant phase transformations and stress space analysis. *Phys. Rev. B* 66, 134207.
- Levitas, V.I., Preston, D.L., 2005. Thermomechanical lattice instability and phase field theory of martensitic phase transformations, twinning and dislocations at large strains. *Phys. Lett. A* 343, 32–39.
- Levitas, V.I., Samani, K., 2011a. Size and mechanics effects in surface-induced melting of nanoparticles. *Nat. Commun.* 2, 284.
- Levitas, V.I., Samani, K., 2011b. Coherent solid–liquid interface with stress relaxation in a phase-field approach to the melting/freezing transition. *Phys. Rev. B* 84, 140103(R).
- Levitas, V.I., Preston, D.L., Lee, D.-W., 2003. Three-dimensional Landau theory for multivariant stress-induced martensitic phase transformations. III. Alternative potentials, critical nuclei, kink solutions, and dislocation theory. *Phys. Rev. B* 68, 134201.
- Levitas, V.I., Idesman, A.V., Preston, D.L., 2004. Microscale simulation of evolution of martensitic microstructure. *Phys. Rev. Lett.* 93, 105701.
- Levitas, V.I., Preston, D.L., Lee, D.-W., 2006a. Ginzburg–Landau theory of microstructures: stability, transient dynamics, and functionally graded nanophases. *Europhys. Lett.* 75, 84–90.
- Levitas, V.I., Levin, V.A., Zingerman, K.M., Freiman, E.I., 2009. Displacive phase transitions at large strains: phase-field theory and simulations. *Phys. Rev. Lett.* 103, 025702.
- Levitas, V.I., Lee, D.-W., Preston, D.L., 2010. Interface propagation and microstructure evolution in phase field models of stress-induced martensitic phase transformations. *Int. J. Plast.* 26, 395–422.
- Levitas, V.I., Idesman, A.V., Stein, E., 1998. Finite element simulation of martensitic phase transitions in elastoplastic materials. *Int. J. Solids Struct.* 35, 855–887.
- Lookman, T., Saxena, A., Albers, R.C., 2008. Phonon mechanisms and transformation paths in Pu. *Phys. Rev. Lett.* 100, 145504.
- Lurie, A.I., 1990. *Nonlinear Theory of Elasticity*. North-Holland.
- Malyushitskaya, Z.V., 1999. Mechanisms responsible for the strain-induced formation of metastable high-pressure Si, Ge, and GaSb phases with distorted tetrahedral coordination. *Inorg. Mater.* 35, 425–430.
- Maple, 2013. <<http://www.maplesoft.com/>>
- Pitteri, M., Zanzotto, G., 2002. *Continuum Models for Phase transitions and Twinning in Crystals*. Chapman and Hall/CRC.
- Rasmussen, K.O., Lookman, T., Saxena, A., Bishop, A.R., Albers, R.C., Shenoy, S.R., 2001. Three-dimensional elastic compatibility and varieties of twins in martensites. *Phys. Rev. Lett.* 87, 055704.
- Reid, A.C.E., Olson, G.B., Moran, B., 1998. Dislocations in nonlinear nonlocal media: martensitic embryo formation. *Phase Transitions* 69, 309–328.
- Rubini, S., Ballone, P., 1993. Quasiharmonic and molecular-dynamics study of the martensitic transformation in Ni–Al alloys. *Phys. Rev. B* 48, 99–111.
- Saxena, A., Wu, Y., Lookman, T., Shenoy, S.R., Bishop, A.R., 1997. Hierarchical pattern formation in elastic materials. *Phys. A* 239, 18–34.
- Seol, D.J., Hu, S.Y., Li, Y.L., Chen, L.Q., Oh, K.H., 2002. Computer simulation of martensitic transformation in constrained films. *Mater. Sci. Forum*, 1645–1650.
- Seol, D.J., Hu, S.Y., Li, Y.L., Chen, L.Q., Oh, K.H., 2003. Cubic to tetragonal martensitic transformation in a thin film elastically constrained by a substrate. *Met. Mater. Int.* 9, 221–226.
- Vedantam, S., Abeyaratne, R., 2005. A Helmholtz free-energy function for a Cu–Al–Ni shape memory alloy. *Int. J. Non Linear Mech.* 40, 177–193.
- Wang, Y., Khachatryan, A.G., 1997. Three-dimensional field model and computer simulation of martensitic transformation. *Acta Mater.* 45, 759–773.
- Zienkiewicz, O.C., Taylor, R.L., 2000a. *The finite element method. The Basis*, vol. 1. Butterworth-Heinemann.
- Zienkiewicz, O.C., Taylor, R.L., 2000b. *The finite element method. Solid Mechanics*, vol. 2. Butterworth-Heinemann.